Interpretation of spacetimes with expanding impulsive gravitational waves generated by snapped cosmic strings

D. Kofroň,[*] M. Karamazov,[†] and R. Švarc[‡]

Institute of Theoretical Physics, Charles University, Faculty of Mathematics and Physics, V Holešovičkách 2, 180 00 Prague 8, Czech Republic

(Received 23 February 2023; accepted 12 July 2023; published 25 August 2023)

Spacetimes representing expanding impulsive gravitational waves propagating on a flat background are studied. The impulses are generated by various configurations of snapped cosmic strings. Employing the previous results [J. Podolský *et al.*, The global uniqueness and C^1-regularity of geodesics in expanding impulsive gravitational waves, Classical Quantum Gravity **33**, 195010 (2016)], analyzing the geodesic motion in generic expanding impulses, we investigate geometric properties of more intricate stringlike wave sources than the standard case of a single snapped string. Such solutions representing pairs of snapping strings were technically derived in Podolský and Griffiths [The collision and snapping of cosmic strings generating spherical impulsive gravitational waves, Classical Quantum Gravity **17**, 1401 (2000)], however, the corresponding physical analysis requires to introduce their generalizations to point out various subtleties in the construction. As the main tool, we thus use the close connection between the spacetime structure and the motion of free test particles crossing the impulse. Within our contribution, the explicit models of a boosted snapped cosmic string and boosted perpendicular or parallel configurations of string pairs are discussed in detail.

DOI: 10.1103/PhysRevD.108.044059

I. INTRODUCTION

Interestingly, the prediction of gravitational waves (GW) became an immediate consequence of Einstein's geometric description of gravity in terms of curved spacetime. The analysis of the weak-field regime [1,2] as well as pioneering studies of invariants within full theory [3,4] pointed out their inherent properties and gave quantitative estimates about the magnitude of typical amplitudes. Simultaneously, it became clear that their observation is going to be very challenging or even impossible. In 1974 Hulse and Taylor discovered the binary pulsar PSR $1913+16$ [5]. The systematic measurements of its orbital period shifts exactly corresponded to the gravitational energy loss radiated away in the form of GWs. This was in perfect agreement with the general relativity (GR) prediction and endorsed the hunt for their direct detection. The unrelenting effort was rewarded in 2015 when the LIGO facility detected a signal produced by merging pair of black holes more than one billion light years away [6]. Until now, dozens of other events have been detected with the prominent case of merging neutron stars [7], where the GW signal was supplemented by observations in the whole range of the electromagnetic spectrum.

These ultimate experimental achievements are based on sophisticated numerical simulations. However, to better understand the GW properties, or to verify various models and numerical schemes, even the exact analytical radiative spacetimes are necessary. The most important wavelike solutions to Einstein's general relativity belong to the expanding Robinson-Trautman and nonexpanding Kundt classes of exact spacetimes [8–11], see [12,13] for the comprehensive review. Interestingly, both these classes allow for the impulsive profiles of the wave, where the propagating curvature is located only on the singular null hypersurface. The impulsive solutions are then interpreted as extremely short, but simultaneously very intense, bursts of gravitational radiation. Technically, it corresponds to the presence of distributional terms in the spacetime geometric quantities. Therefore, these geometries are also of purely mathematical interest since careful manipulation with inherently non-linear distributional terms is required that necessarily goes beyond the classical theory, see e.g., [14,15].

Within this paper, we are interested in the expanding Robinson-Trautman impulses propagating on a flat Minkowski background. It is worth mentioning that the elegant geometric construction of these models goes back to the seventies when Roger Penrose proposed the "cut and paste" approach [16]. Two decades later Penrose and Nutku found the continuous line element for these solutions [17]. Subsequently, various extensions and applications of such a

[*]d.kofron@gmail.com
[†]michal.karamazov@gmail.com
[‡]robert.svarc@mff.cuni.cz

construction were presented, e.g., including the cosmological constant or other additional parameters [18–23]. The historical content, summary of other construction methods (e.g., limits of expanding sandwich waves or infinite acceleration limit of the C-metric), and detailed list of references can be found, e.g., in [13,24,25]. In the original work [17], the snapped cosmic string serving as a wave source was described and the possibility of impulses generated by a pair of colliding and snapping strings was outlined. This scenario was elaborated by Podolský and Griffiths [26]. However, the complete understanding of the spacetime topology remained an open problem, since at that time the suitable tools for such an analysis within spacetimes of low regularity were not developed. Simultaneously, based on the simple one-string case, the topology seems to play a crucial role in the behavior of free test particles affected by the expanding gravitational impulse, and vice versa, the geodesic motion reflects the spacetime geometry [27,28]. The studies of one-string geodesics were put on a solid rigorous ground later in [25] assuming a fully general expanding impulses. However, these theoretical results were lacking for their explicit applications going beyond the simplest case [28].

Therefore, the present contribution aims to combine the previous results, mainly [25,26,28], and discuss properties of selected stringlike sources of the expanding impulses in terms of the induced geodesic motion. This provides a direct insight into the properties of such impulsive geometries. As we have already mentioned, such an analysis could have been a very natural supplement already to the original works, however, there were no suitable methods to do so. We thus fill this gap. Moreover, the physical interpretations of solutions obtained in [26] in terms of the geodesics motion following [25] requires their generalization simultaneously uncovering several subtleties of the construction. To make our contribution self-consistent we briefly summarize all necessary previous results. In particular, in Sec. II, the expanding impulsive waves are described based on the original papers [16,17,25]. Subsequently, the elements of construction of stringlike geometries are reviewed in Sec. III following mainly [26]. The description of geodesics derived in [28] and rigorously justified in [25] is presented in Sec. IV. The new results generalizing the original complex mapping of [26] are then contained in the Secs. V and VI, where we simultaneously discuss and interpret specific properties of one and two-string geometries, respectively, employing the analysis of the interaction of free-test particles with corresponding gravitational impulses.

II. EXPANDING GRAVITATIONAL IMPULSES ON A FLAT BACKGROUND

Here, we follow the original works [16,17] and the comprehensive review [25] to summarize the construction of expanding gravitational impulses. It is natural to begin with a description of the Penrose geometric "cut and paste" method in the simplest situation of an expanding impulse propagating on a flat Minkowski background

$$\mathrm{d}s^2 = -\mathrm{d}t^2 + \mathrm{d}x^2 + \mathrm{d}y^2 + \mathrm{d}z^2, \tag{1}$$

which can be simply rewritten using the double null coordinates,

$$t = \frac{1}{\sqrt{2}}(\mathcal{V}+\mathcal{U}), \qquad z = \frac{1}{\sqrt{2}}(\mathcal{V}-\mathcal{U}),$$
$$x = \frac{1}{\sqrt{2}}(\eta+\bar{\eta}), \qquad y = \frac{1}{i\sqrt{2}}(\eta-\bar{\eta}), \tag{2}$$

to the form

$$\mathrm{d}s^2 = -2\mathrm{d}\mathcal{U}\mathrm{d}\mathcal{V} + 2\mathrm{d}\eta\mathrm{d}\bar{\eta}. \tag{3}$$

Applying further transformation to the Minkowski metric (3),

$$\mathcal{V} = \frac{V}{p} - \epsilon U, \quad \mathcal{U} = \frac{|Z|^2}{p}V - U, \quad \eta = \frac{Z}{p}V, \tag{4}$$

with

$$p = 1 + \epsilon Z\bar{Z}, \quad \text{where } \epsilon = -1, 0, +1, \tag{5}$$

we get the line element

$$\mathrm{d}s^2 = 2\frac{V^2}{p^2}\mathrm{d}Z\mathrm{d}\bar{Z} + 2\mathrm{d}U\mathrm{d}V - 2\epsilon\mathrm{d}U^2, \tag{6}$$

which explicitly describes the foliation of the flat spacetime by null cones that are labeled by constant values of the coordinate U. The parameter ϵ encodes the Gaussian curvature of spatial two-surfaces $U = \text{const}$ and $V = \text{const}$, see [13] for the detailed geometric picture.

However, another more involved transformation of (3) can be performed (simultaneously leading to the explicit null-cone foliation), namely

$$\mathcal{V} = AV - DU, \quad \mathcal{U} = BV - EU, \quad \eta = CV - FU, \tag{7}$$

where

$$A=\frac{1}{p|h'|},\qquad D=\frac{1}{|h'|}\left\{\frac{p}{4}\left|\frac{h''}{h'}\right|^2+\epsilon\left[1+\frac{Z}{2}\frac{h''}{h'}+\frac{\bar{Z}}{2}\frac{\bar{h}''}{\bar{h}'}\right]\right\},$$
$$B=\frac{|h|^2}{p|h'|},\qquad E=\frac{|h|^2}{|h'|}\left\{\frac{p}{4}\left|\frac{h''}{h'}-2\frac{h'}{h}\right|^2+\epsilon\left[1+\frac{Z}{2}\left(\frac{h''}{h'}-2\frac{h'}{h}\right)+\frac{\bar{Z}}{2}\left(\frac{\bar{h}''}{\bar{h}'}-2\frac{\bar{h}'}{\bar{h}}\right)\right]\right\},$$
$$C=\frac{h}{p|h'|},\qquad F=\frac{h}{|h'|}\left\{\frac{p}{4}\left(\frac{h''}{h'}-2\frac{h'}{h}\right)\frac{\bar{h}''}{\bar{h}'}+\epsilon\left[1+\frac{Z}{2}\left(\frac{h''}{h'}-2\frac{h'}{h}\right)+\frac{\bar{Z}}{2}\frac{\bar{h}''}{\bar{h}'}\right]\right\},\tag{8}$$

with $h=h(Z)$ representing an arbitrary complex holomorphic function (apart from its singular points) and a prime denoting its derivative. The resulting line element becomes

$$\mathrm{d}s^2=2\left|\frac{V}{p}\mathrm{d}Z+Up\bar{H}\mathrm{d}\bar{Z}\right|^2+2\mathrm{d}U\mathrm{d}V-2\epsilon\mathrm{d}U^2,\tag{9}$$

where H is the Schwarzian derivative of the function h defined as

$$H(h(Z))\equiv\frac{1}{2}\left[\frac{h'''}{h'}-\frac{3}{2}\left(\frac{h''}{h'}\right)^2\right].\tag{10}$$

Although the metric (9) still represents the flat space, the nontriviality of function H leads to the topological defects primarily induced by the choice of its generator $h(Z)$.

Finally, to construct the expanding impulsive gravitational wave on a flat background one has to cut the Minkowski spacetime along the null cone and then reattached the two half-spaces with an appropriate warp, see Fig. 1. Using the coordinates of (6) and taking the null cone $U=0$, corresponding to the expanding sphere $t^2=x^2+y^2+z^2$, the half-spaces $\mathcal{M}^-$ (with $U\leq 0$) and $\mathcal{M}^+$ (with $U\geq 0$) have to be identified across the null hypersurface $\mathcal{N}$ as

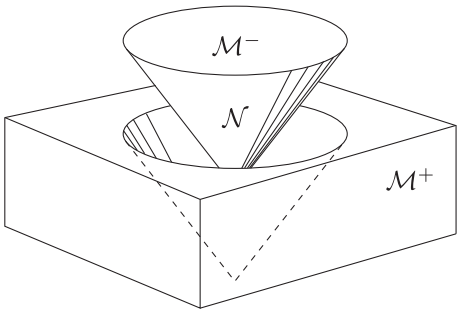

FIG. 1. Two parts $\mathcal{M}^-$ and $\mathcal{M}^+$ of the flat Minkowski background are re-attached along a future-oriented null cone $\mathcal{N}$ with a suitable warp given by the junction Penrose conditions (11). Such construction results in the presence of expanding spherical gravitational impulse located on $\mathcal{N}$ whose specific nature is encoded in the (holomorphic) function $h(Z)$ identifying points of $\mathcal{M}^-$ and $\mathcal{M}^+$ across $\mathcal{N}$.

$$[Z,\bar{Z},V,U=0_-]_{\mathcal{M}^-}\equiv\left[h(Z),\bar{h}(\bar{Z}),\frac{1+\epsilon h\bar{h}}{1+\epsilon Z\bar{Z}}\frac{V}{|h'|},U=0_+\right]_{\mathcal{M}^+}.\tag{11}$$

The Penrose junction conditions directly correspond to the evaluation of transformations (4) and (7), respectively, on the impulse $U=0$, i.e., $\mathcal{U}\mathcal{V}-\eta\bar{\eta}=0$. The global continuous line element can be then written as a combination of (6) and (9), namely

$$\mathrm{d}s^2=2\left|\frac{V}{p}\mathrm{d}Z+U\Theta(U)p\bar{H}\mathrm{d}\bar{Z}\right|^2+2\mathrm{d}U\mathrm{d}V-2\epsilon\mathrm{d}U^2,\tag{12}$$

where the product of U and Heaviside step $\Theta(U)$ represents the continuous kink function which is typically denoted as $U_+\equiv U\Theta(U)$. The metric (12) then solves the vacuum Einstein field equations everywhere except at the singular impulse origin ($U=0=V$), and possible poles of p^2H as can be inferred from the curvature invariants, see e.g., [25].

III. GEOMETRY OF EXPANDING IMPULSES

In this section we discuss the specific contributions to the warp function $h(Z)$ representing the source of an expanding impulse. The standard parametrization of Lorentz transformations and conical singularities is used as, e.g., in the original work [26], however, we adapt the notation to allow for a more algorithmic approach. Concerning the Schwarzian derivative (10), the wavelike nature of $h(Z)$ can be distinguished. In particular, the general Möbius transformation of the complex plane to itself,

$$h(Z):Z\mapsto\frac{aZ+b}{cZ+d},\tag{13}$$

leaves $H(h(Z))$ unchanged and corresponds to the simple Lorentz transformation. On the other hand, going beyond the linear fractional transformation brings the nontrivial Schwarzian derivative. In our case, it will be interpreted as a topological defect related to the presence of cosmic string. To geometrically describe these effects in the flat Minkowski space, it is useful to employ stereographic projection, see e.g., [26]. The mapping $Z\mapsto h(Z)$ in the complex Argand plane corresponds to the geometric

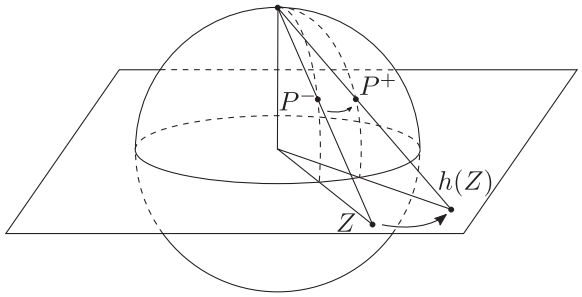

FIG. 2. Stereographic projection corresponds to the mutual identification between points of the Riemann sphere and complex Argand plane. In the case of expanding impulses, it gives direct geometric interpretation to the holomorphic mapping $h(Z)$ and the Penrose junction conditions (11).

identifications of points P^- and P^+ on a Riemann sphere, see Fig. 2. The Riemann sphere can be further identified within the background Cartesian coordinates. In particular, taking the continuous metric (12) and the coordinate transformations leading to the half-spaces in front of $(U \geq 0)$ and behind $(U \leq 0)$ the impulse, respectively, we find that the impulsive surface $U = 0$ is a sphere $(t_{\mathrm{i}}^{\pm})^2 = (x_{\mathrm{i}}^{\pm})^2 + (y_{\mathrm{i}}^{\pm})^2 + (z_{\mathrm{i}}^{\pm})^2$, where the $\pm$ sign corresponds to a specific half-space from which $\mathcal{N}$ is approached, and the index $_{\mathrm{i}}$ indicates values obtained on the impulse $\mathcal{N}$, i.e., on $U = 0$. Then, we get

$$Z_{\mathrm{i}} = \frac{\eta_{\mathrm{i}}^-}{\mathcal{V}_{\mathrm{i}}^-} = \frac{x_{\mathrm{i}}^- + iy_{\mathrm{i}}^-}{t_{\mathrm{i}}^- + z_{\mathrm{i}}^-}, \quad h(Z_{\mathrm{i}}) = \frac{\eta_{\mathrm{i}}^+}{\mathcal{V}_{\mathrm{i}}^+} = \frac{x_{\mathrm{i}}^+ + iy_{\mathrm{i}}^+}{t_{\mathrm{i}}^+ + z_{\mathrm{i}}^+}. \tag{14}$$

Inversely, we can write

$$\frac{x_{\mathrm{i}}^-}{t_{\mathrm{i}}^-} = \frac{Z_{\mathrm{i}} + \bar{Z}_{\mathrm{i}}}{1 + |Z_{\mathrm{i}}|^2}, \quad \frac{y_{\mathrm{i}}^-}{t_{\mathrm{i}}^-} = -i\frac{Z_{\mathrm{i}} - \bar{Z}_{\mathrm{i}}}{1 + |Z_{\mathrm{i}}|^2}, \quad \frac{z_{\mathrm{i}}^-}{t_{\mathrm{i}}^-} = \frac{1 - |Z_{\mathrm{i}}|^2}{1 + |Z_{\mathrm{i}}|^2}, \tag{15}$$

$$\frac{x_{\mathrm{i}}^+}{t_{\mathrm{i}}^+} = \frac{h + \bar{h}}{1 + |h|^2}, \quad \frac{y_{\mathrm{i}}^+}{t_{\mathrm{i}}^+} = -i\frac{h - \bar{h}}{1 + |h|^2}, \quad \frac{z_{\mathrm{i}}^+}{t_{\mathrm{i}}^+} = \frac{1 - |h|^2}{1 + |h|^2}, \tag{16}$$

where the function h is evaluated at Z_{i}. The expressions (15) and (16) can thus be understood as the stereographic identification between points in the complex plane and their images on a unit Riemann sphere representing the rescaled impulsive surface. Subsequently, in terms of such a unit sphere endowed with the Cartesian axes, one can interpret the effects of mapping $h(Z)$.

In particular, the construction of explicit form of the function $h(Z)$ can be decomposed into operations representing either pure Lorentz transformations of the form (13) or mappings inducing nontrivial Schwartzian derivative (10). Here, let us define elementary operations which will be sequentially applied within the following discussion:

(i) the natural starting point is an identical mapping,[1] i.e.,

$$h_0(Z) = Z; \tag{17}$$

(ii) the spatial rotations $\mathcal{R}_{\{\varphi,\vartheta,\psi\}}$ parametrized by the Euler angles $\{\varphi, \vartheta, \psi\}$ lead to

$$h_{j+1}(Z) = \mathcal{R}_{\{\varphi,\vartheta,\psi\}} h_j(Z) = e^{i\varphi} \frac{-\sin(\vartheta/2) + e^{i\psi}\cos(\vartheta/2) h_j}{\cos(\vartheta/2) + e^{i\psi}\sin(\vartheta/2) h_j}, \tag{18}$$

see the left part of Fig. 3 representing the rotated Riemann sphere;

(iii) the Lorentz boost in the direction of the z-axis $\mathcal{B}_{\{w\}}$, parametrized by the value w, gives

$$h_{j+1}(Z) = \mathcal{B}_{\{w\}} h_j(Z) = w h_j(Z), \tag{19}$$

see the middle plots in Fig. 3 for a pure boost and its combination with a rotation (18); and

(iv) finally, the simplest stringlike structure can be constructed by "cutting" out the wedge $2\pi\delta$ around z-axis, represented by the action of $\mathcal{S}_{\{\delta\}}$, namely

$$h_{j+1}(Z) = \mathcal{S}_{\{\delta\}} h_j(Z) = [h_j(Z)]^{1-\delta}, \tag{20}$$

where the wedge is missing symmetrically in the direction of the negative x-axis, see the last example in Fig. 3. To be more precise, this operation does not only remove a given angle. However, the spherical surface is cut along the z–x plane (for the negative x values) and then the angle $2\pi\delta$ is opened, while the surface is "compressed" (as an accordion or a paper lantern), which may affect already existing defects as we show later.

These operations have to be understood as the active transformations of the sphere, while the coordinate system and axes are kept fixed. In general, the Euler angles are arbitrary and it thus seems to be possible to cut out an arbitrary number of strings along different axes, which are moving with different velocities. We will show explicit examples below. Finally, the elementary operations (17)–(20) could be supplemented with other operations, e.g., boosts in the x- and y-directions. However, these additional operations can be simply understood as their compositions.

IV. INTERACTION OF GEODESICS WITH THE EXPANDING IMPULSES

We aim to analyze properties of particular expanding impulses prescribed by explicit choices of the generating

[1]The subscript $_j$ of $h_j(Z)$ identifies particular step in a sequence of the final $h(Z)$ construction.

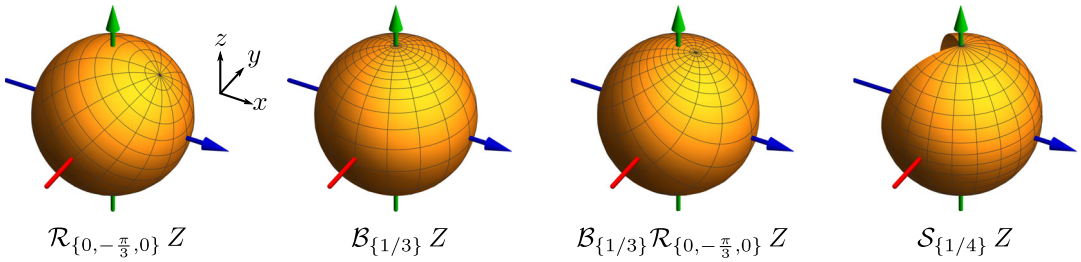

FIG. 3. Visualization of specific elementary operations acting on the whole Riemann sphere associated with the rescaled impulsive surface. Their combinations enter the construction of a particular form of the function $h(Z)$ that, subsequently, encodes the geometric nature of a given expanding impulsive wave described by (12).

function $h(Z)$, see Secs. V and VI. Such a discussion is closely related to the geodesic motion of test observers affected by interaction with the gravitational impulse. However, due to the presence of a kink function in the continuous metric (12), the distributional terms appear in the geodesic equation and its analysis becomes more tricky. The particular case of $Z=\text{const}$ geodesics was studied in [27]. Assuming the C^1 geodesics, the refraction formulas for their interaction with a generic impulse were derived in [28]. Subsequently, the existence and global uniqueness of such C^1 geodesics crossing an expanding impulse, propagating on all constant curvature backgrounds, was rigorously proved in [25,29] using the Filippov solution concept [30,31]. Such refraction formulas connect initial data $\{\mathcal{U}_{\rm i}^+,\mathcal{V}_{\rm i}^+,\eta_{\rm i}^+,\dot{\mathcal{U}}_{\rm i}^+,\dot{\mathcal{V}}_{\rm i}^+,\dot{\eta}_{\rm i}^+\}$ and $\{\mathcal{U}_{\rm i}^-,\mathcal{V}_{\rm i}^-,\eta_{\rm i}^-,\dot{\mathcal{U}}_{\rm i}^-,\dot{\mathcal{V}}_{\rm i}^-,\dot{\eta}_{\rm i}^-\}$ for the straight lines parametrized by τ, namely

$$\begin{aligned}\mathcal{U}^\pm(\tau)&=\dot{\mathcal{U}}_{\rm i}^\pm\tau+\mathcal{U}_{\rm i}^\pm,\\ \mathcal{V}^\pm(\tau)&=\dot{\mathcal{V}}_{\rm i}^\pm\tau+\mathcal{V}_{\rm i}^\pm,\\ \eta^\pm(\tau)&=\dot{\eta}_{\rm i}^\pm\tau+\eta_{\rm i}^\pm,\end{aligned}\tag{21}$$

i.e., geodesics in the Minkowski half-spaces $\mathcal{M}^+$ and $\mathcal{M}^-$, starting/ending on the impulse $\mathcal{N}$ at $\tau=0$, see (22) and (23) below.

Here, let us summarize the main result of [25,28] which is important for our further discussion. The explicit C^1 matching of geodesics crossing the impulse can be expressed in the form of the refraction formulas encoding the shift of positions and change of the velocities with respect to the fiducial interpretative background. These are derived starting from the fact that the geodesics in coordinates (12) are unique C^1 lines across the impulsive wave front $\mathcal{N}$ given by $U=0$, i.e., components of position and velocity evaluated on the impulsive boundary $\mathcal{N}$ (denoted by the subscript "i") are the same irrespectively whether $\mathcal{N}$ is approached from the region $\mathcal{M}^+$ with $U\geq 0$ (denoted by the superscript "+") or from the complementary half-space $\mathcal{M}^-$ with $U\leq 0$ (denoted by the superscript "−"). However, to observe the influence of the impulse on test particles, it is natural to employ the fiducial background coordinates (3) for $\mathcal{M}^+$ and $\mathcal{M}^-$, respectively. With respect to the background space, the global geodesics do not cross the impulse continuously and the effects of impulse on their motion become explicit. In particular, evaluation of the transformations (4) and (7) on $U=0$, and elimination of the continuous coordinates, gives the position shift,

$$\mathcal{U}_{\rm i}^-=|h'|\frac{|Z_{\rm i}|^2}{|h|^2}\mathcal{U}_{\rm i}^+,\quad \mathcal{V}_{\rm i}^-=|h'|\mathcal{V}_{\rm i}^+,\quad \eta_{\rm i}^-=|h'|\frac{Z_{\rm i}}{h}\eta_{\rm i}^+,\tag{22}$$

while the same procedure for derivatives of (4) and (7) leads to the refraction of the velocities,

$$\begin{aligned}\dot{\mathcal{U}}_{\rm i}^-&=a_{\mathcal{U}}\dot{\mathcal{U}}_{\rm i}^+ +b_{\mathcal{U}}\dot{\mathcal{V}}_{\rm i}^+ +\bar{c}_{\mathcal{U}}\dot{\eta}_{\rm i}^+ +c_{\mathcal{U}}\dot{\bar{\eta}}_{\rm i}^+,\\ \dot{\mathcal{V}}_{\rm i}^-&=a_{\mathcal{V}}\dot{\mathcal{U}}_{\rm i}^+ +b_{\mathcal{V}}\dot{\mathcal{V}}_{\rm i}^+ +\bar{c}_{\mathcal{V}}\dot{\eta}_{\rm i}^+ +c_{\mathcal{V}}\dot{\bar{\eta}}_{\rm i}^+,\\ \dot{\eta}_{\rm i}^-&=a_{\eta}\dot{\mathcal{U}}_{\rm i}^+ +b_{\eta}\dot{\mathcal{V}}_{\rm i}^+ +\bar{c}_{\eta}\dot{\eta}_{\rm i}^+ +c_{\eta}\dot{\bar{\eta}}_{\rm i}^+,\end{aligned}\tag{23}$$

where the coefficients are constants evaluated on $\mathcal{N}$ with $Z_{\rm i}$ obtained via $h(Z_{\rm i})=\frac{\eta_{\rm i}^+}{\mathcal{V}_{\rm i}^+}$, namely

$$a_{\mathcal{U}}=\frac{1}{|h'|}\left|1+\frac{Z_{\rm i}}{2}\frac{h''}{h'}\right|^2,\tag{24}$$

$$a_{\mathcal{V}}=\frac{1}{4|h'|}\left|\frac{h''}{h'}\right|^2,\tag{25}$$

$$a_{\eta}=\frac{1}{2|h'|}\left(1+\frac{Z_{\rm i}}{2}\frac{h''}{h'}\right)\frac{\bar{h}''}{\bar{h}'},\tag{26}$$

$$b_{\mathcal{U}}=\frac{|h|^2}{|h'|}\left|1+\frac{Z_{\rm i}}{2}\left(\frac{h''}{h'}-2\frac{h'}{h}\right)\right|^2,\tag{27}$$

$$b_{\mathcal{V}}=\frac{|h|^2}{4|h'|}\left|\frac{h''}{h'}-2\frac{h'}{h}\right|^2,\tag{28}$$

$$b_{\eta}=\frac{|h|^2}{2|h'|}\left[1+\frac{Z_{\rm i}}{2}\left(\frac{h''}{h'}-2\frac{h'}{h}\right)\right]\left(\frac{\bar{h}''}{\bar{h}'}-2\frac{\bar{h}'}{\bar{h}}\right),\tag{29}$$

$$c_{\mathcal{U}} = -\frac{h}{|h'|}\left[1+\frac{Z_\mathrm{i}}{2}\left(\frac{h''}{h'}-2\frac{h'}{h}\right)\right]\left[1+\frac{\bar{Z}_\mathrm{i}}{2}\frac{\bar{h}''}{\bar{h}'}\right], \tag{30}$$

$$c_{\mathcal{V}} = -\frac{h}{4|h'|}\left(\frac{h''}{h'}-2\frac{h'}{h}\right)\frac{\bar{h}''}{\bar{h}'}, \tag{31}$$

$$c_{\eta} = -\frac{h}{2|h'|}\left[1+\frac{Z_\mathrm{i}}{2}\left(\frac{h''}{h'}-2\frac{h'}{h}\right)\right]\frac{\bar{h}''}{\bar{h}'}, \tag{32}$$

$$\bar{c}_{\eta} = -\frac{\bar{h}}{2|h'|}\left(1+\frac{Z_\mathrm{i}}{2}\frac{h''}{h'}\right)\left(\frac{\bar{h}''}{\bar{h}'}-2\frac{\bar{h}'}{\bar{h}}\right). \tag{33}$$

Notice that $\bar{c}_{\mathcal{V}} = \overline{c_{\mathcal{V}}}$, $\bar{c}_{\mathcal{U}} = \overline{c_{\mathcal{U}}}$. As shown in [25], the normalization of velocity is preserved across the impulse, i.e., $\dot{\eta}_\mathrm{i}^- \dot{\bar{\eta}}_\mathrm{i}^- - \dot{\mathcal{U}}_\mathrm{i}^- \dot{\mathcal{V}}_\mathrm{i}^- = \dot{\eta}_\mathrm{i}^+ \dot{\bar{\eta}}_\mathrm{i}^+ - \dot{\mathcal{U}}_\mathrm{i}^+ \dot{\mathcal{V}}_\mathrm{i}^+$. The above (local) expressions do not depend on the Gaussian curvature ϵ, however, to construct a global picture the parameter ϵ encoding the spacetime foliation has to be considered, see [13,25]. The refraction formulas become identical in the trivial case $h(Z) = Z$ that implies $H = 0$ and lacks the impulse. However, one should be careful in the case of nontrivial $h(Z)$ and still trivial $H = 0$, where the above expressions identify two Minkowski half-spaces via Möbius transformation (13), see Sec. VI. This ambiguity in mutual background Cartesian coordinate identification on both sides of the impulse, nonphysically affecting in the above refraction formulas, arises from the absence of global Cartesian-like impulsive metric for the expanding waves in contrast to the nonexpanding case, see e.g., [32].

To identify the pure-wave action on the test observers, a specific choice of the initial data $\{\mathcal{U}_\mathrm{i}^+, \mathcal{V}_\mathrm{i}^+, \eta_\mathrm{i}^+, \dot{\mathcal{U}}_\mathrm{i}^+, \dot{\mathcal{V}}_\mathrm{i}^+, \dot{\eta}_\mathrm{i}^+\}$ has to be made which enters the above expressions. Due to the time shift given by a combination of (2) and (22), we can naturally consider either a swarm of test particles which is hit by the impulsive wave front $\mathcal{N}$ at the same constant coordinate time t_i^+ in $\mathcal{M}^+$, or vice versa, which appears in the region $\mathcal{M}^-$ simultaneously at constant coordinate time t_i^-. The second possibility can be also understood as the case of an impulse passing through the continuous dustlike distribution of particles where we observe one fixed-emergence slice given by constant time t_i^-. To emphasize the geometric effect of the particular impulse realization encoded in the mapping $h(Z)$, we will assume test particles at rest in $\mathcal{M}^+$ (the rest is defined with respect to the background Minkowskian coordinates, i.e., $\dot{\mathcal{U}}_\mathrm{i}^+ = \dot{\mathcal{V}}_\mathrm{i}^+ = \dot{\eta}_\mathrm{i}^+ = 0$), which are spherically distributed at radii $t_\mathrm{i}^+ = \mathrm{const}$ or $t_\mathrm{i}^- = \mathrm{const}$, respectively. A schematic visualization of the above cases (in the simplest one-string situation) is given in Fig. 4. The explicit initial data constraints are summarized in the following subsections.

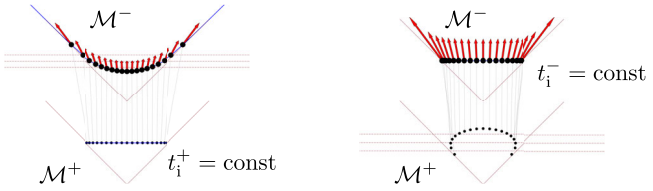

FIG. 4. A swarm of particles at rest in $\mathcal{M}^+$ hit by the typical expanding impulse (null cone $\mathcal{N}$) as seen from the half-space $\mathcal{M}^+$ (lower part of the schema) and its emergence at the null cone $\mathcal{N}$ as seen from the half-space $\mathcal{M}^-$ (upper part of the schema). On the left, the test particles interact with the impulse at $t_\mathrm{i}^+ = \mathrm{const}$ while the right part is the case with $t_\mathrm{i}^- = \mathrm{const}$. In this particular case, it can be seen that the particles attain a radial component of the velocity being "attracted" to the axis at the time they leave the wave which causes a formation of caustics later.

A. Spheres in front of the wave

A Cartesian sphere (formed by test particles) of a constant radius t_i^+ in front of the wave corresponds to the particle's displacement on a particular cut of the null impulsive cone $U = 0$ encoded in specific values of the global coordinate V_i at the instant of interaction. In particular, evaluation of the transformation (7) with (2) on the null cone $U = 0$ gives the constraint

$$t_\mathrm{i}^+ = \frac{V_\mathrm{i}}{\sqrt{2}|h'|}\frac{1+|h|^2}{1+\epsilon|Z_\mathrm{i}|^2} = \mathrm{const}, \tag{34}$$

which, combined with the initial assumption $t_\mathrm{i}^+ = \mathrm{const}$, fixes the values V_i for specific choices of complex plane positions $h(Z_\mathrm{i})$ (and inversely Z_i). The $h(Z_\mathrm{i})$ value is related to the Cartesian parametrization via stereographic projection (16),

$$x_\mathrm{i}^+ = \frac{h+\bar{h}}{1+|h|^2}t_\mathrm{i}^+, \quad y_\mathrm{i}^+ = -i\frac{h-\bar{h}}{1+|h|^2}t_\mathrm{i}^+, \quad z_\mathrm{i}^+ = \frac{1-|h|^2}{1+|h|^2}t_\mathrm{i}^+. \tag{35}$$

In the case of nontrivial $h(Z)$ with respect to its Schwartzian derivative (10), the Cartesian image will suffer for different cutouts. At this moment, it is useful to adopt natural parametrization,

$$Z_\mathrm{i} = \tan\frac{\theta}{2}e^{i\phi}, \tag{36}$$

so that $(x_\mathrm{i}^\pm, y_\mathrm{i}^\pm, z_\mathrm{i}^\pm)$ are functions of $\theta \in [0,\pi)$ and $\phi \in [-\pi,\pi)$. Subsequently, the deformation of such a test ball is explicitly described by the shift of positions (22), or directly in terms of the continuous coordinates using the stereographic projection (15) of null cone $\mathcal{N}$ as viewed from the region behind the impulse. The scale in terms of the original constant radius t_i^+ is given by

$$t_\mathrm{i}^- = \frac{V_\mathrm{i}}{\sqrt{2}}\frac{1+|Z_\mathrm{i}|^2}{1+\epsilon|Z_\mathrm{i}|^2} = |h'|\frac{1+|Z_\mathrm{i}|^2}{1+|h|^2}t_\mathrm{i}^+, \tag{37}$$

while the deformed surface in front of the wave can be plotted as

$$x_{\rm i}^- = |h'|\frac{Z_{\rm i}+\bar{Z}_{\rm i}}{1+|h|^2}t_{\rm i}^+, \qquad y_{\rm i}^- = -i|h'|\frac{Z_{\rm i}-\bar{Z}_{\rm i}}{1+|h|^2}t_{\rm i}^+,$$
$$z_{\rm i}^- = |h'|\frac{1-|Z_{\rm i}|^2}{1+|h|^2}t_{\rm i}^+, \tag{38}$$

which still satisfy $(x_{\rm i}^-)^2+(y_{\rm i}^-)^2+(z_{\rm i}^-)^2=(t_{\rm i}^-)^2$, however, $t_{\rm i}^-$ is no more a constant.

B. Spheres behind the wave

The second very natural choice of the initial data is such that the test particles form a sphere at a given constant time $t_{\rm i}^-$ behind the wave, i.e., in the region without any strings. The null cone cut is fixed in terms of values $V_{\rm i}$ of the global coordinate V by the condition

$$t_{\rm i}^- = \frac{V_{\rm i}}{\sqrt{2}}\frac{1+|Z_{\rm i}|^2}{1+\epsilon|Z_{\rm i}|^2} = \text{const}, \tag{39}$$

and the Cartesian positions on a sphere are related to the values $Z_{\rm i}$ by (15),

$$x_{\rm i}^- = \frac{Z_{\rm i}+\bar{Z}_{\rm i}}{1+|Z_{\rm i}|^2}t_{\rm i}^-, \quad y_{\rm i}^- = -i\frac{Z_{\rm i}-\bar{Z}_{\rm i}}{1+|Z_{\rm i}|^2}t_{\rm i}^-, \quad z_{\rm i}^- = \frac{1-|Z_{\rm i}|^2}{1+|Z_{\rm i}|^2}t_{\rm i}^-. \tag{40}$$

Viewed from the region $U>0$, this corresponds to the deformed initial displacement given by (16) satisfying $(x_{\rm i}^+)^2+(y_{\rm i}^+)^2+(z_{\rm i}^+)^2=(t_{\rm i}^+)^2$ with nonconstant scaling

$$t_{\rm i}^+ = \frac{V_{\rm i}}{\sqrt{2}|h'|}\frac{1+|h|^2}{1+\epsilon|Z_{\rm i}|^2} = \frac{1}{|h'|}\frac{1+|h|^2}{1+|Z_{\rm i}|^2}t_{\rm i}^-, \tag{41}$$

and Cartesian positions given by

$$x_{\rm i}^+ = \frac{1}{|h'|}\frac{h+\bar{h}}{1+|Z_{\rm i}|^2}t_{\rm i}^-, \qquad y_{\rm i}^+ = -\frac{i}{|h'|}\frac{h-\bar{h}}{1+|Z_{\rm i}|^2}t_{\rm i}^-,$$
$$z_{\rm i}^+ = \frac{1}{|h'|}\frac{1-|h|^2}{1+|Z_{\rm i}|^2}t_{\rm i}^-. \tag{42}$$

The resulting deformed displacement in $\mathcal{M}^+$ contains defects given by a particular choice of $h(Z)$.

C. Visualizations and location of strings

Although the deformations (35) and (42), respectively, do not depend on the value of the Gaussian curvature ϵ, it is natural to assume the choice $\epsilon=1$. This way, the cuts of the null cone $U=0$, $V_{\rm i}=\text{const}$, parametrized by the remaining global coordinate values $Z_{\rm i}$, are manifestly spheres behind the wave. The radius is $t_{\rm i}^-$ proportional only to $V_{\rm i}$, namely $(x_{\rm i}^-)^2+(y_{\rm i}^-)^2+(z_{\rm i}^-)^2=\frac{1}{2}V_{\rm i}^2$, see (39). This assumption allows for simpler visualizations in terms of the schematic cut and paste Fig. 1, while other choices of ϵ lead to more complicated sections of the null cone.

To understand the resulting geometry it is natural to investigate where the string ends are attached to the null cone. Their location is related to the scaling factors $t_{\rm i}^\pm$. In particular, in the case of initial configuration representing a constant sphere in front of the wave, see Sec. IV A, these points correspond to the divergence of $t_{\rm i}^-$ given by (37), while for the constant sphere behind the impulse, see Sec. IV B, we are inversely looking for zeros of $t_{\rm i}^+$ given by (41). They thus represent extremes of the "radial" distance of the deformed "spherical" surface.

Determination of the string positions allows to distinguish qualitatively different physical situations. For example, we can arrive at the same string configurations by applying the elementary operations in a different order. However, this typically leads to the different forms of the generating function $h(Z)$. Analogously, the rotations will also not change the mutual string configurations, but the functions $h(Z)$ will differ. This can be solved by finding the string ends. Therefore, we map the constant spherelike configuration to obtain its deformed image behind the wave and find points of divergence on such a surface. Then, we can measure mutual angles between all possible pairs of such points for particular functions $h(Z)$. Two configurations are identical if angles agree in both cases.

Finally, keep in mind that we infer all the information about the strings from the behaviour on the null cone or properties of its spherical cuts. To proceed more explicitly, the coordinates (9) in front of the wave, where the strings are present (and, possibly, moving), should be employed in the whole space. However, they are extremely complicated and their analytic inversion to the Cartesian coordinate system, where the topological defects can be directly interpreted, seems to be impossible since it requires finding the inverse of (7) with (8).

V. ONE-STRING GEOMETRIES

Although the one-string case has been frequently studied, we would like to provide its description to point out the important technical aspects of the construction that will subsequently appear in more involved two-string cases. The simplest situation of one string located along the z-axis, and therefore inducing the deficit angle $2\pi\delta$ around it, is given by the mapping

$$h(Z) = Z^{1-\delta}. \tag{43}$$

As we have already mentioned in Sec. IV, test particles forming an initial spherical shell in the region $\mathcal{M}^+$, and interacting with the impulse simultaneously at a constant time $t_{\rm i}^+$, will be displaced in both the space and time

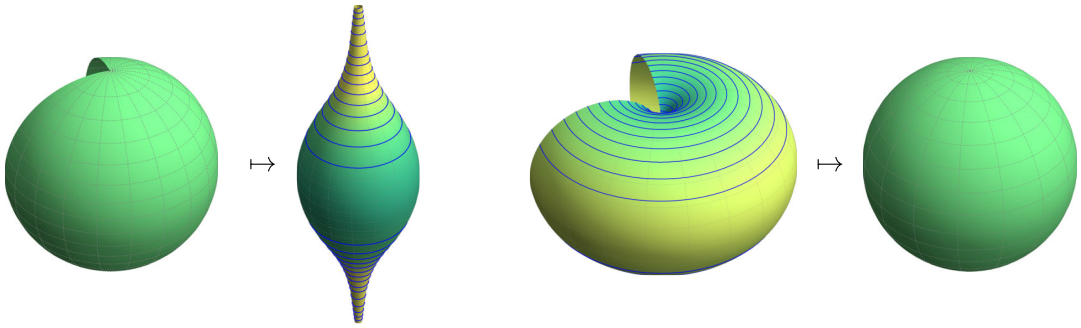

FIG. 5. In part (a+), the test particles are chosen to form a sphere of a constant radius t_i^+ and deficit angle $2\pi\delta$ along z-axis in the region $\mathcal{M}^+$ (in front of the wave). The "sphere" is embedded in the Euclidean space with Cartesian coordinates (x_i^+, y_i^+, z_i^+). The thin dashed lines represent lines of constant θ and ϕ of the stereographic projection (36). This sphere is distorted behind the wave in (x_i^-, y_i^-, z_i^-) coordinates as visualized in part (a−). The particles appear at different times and different locations, see (22). The time shift is depicted by a color change ranging from green to yellow and the lines of constant t_i^- are shown as thick blue lines. There is a singularity along the z-axis (the spikes reach infinity) while the deficit angle disappears. The part (b+) represents such initial conditions in $\mathcal{M}^+$ that the particles emerge as a real geometric sphere in $\mathcal{M}^-$ with radius $t_i^- = \text{const}$ and coordinates (x_i^-, y_i^-, z_i^-), see part (b−). In (b+) the same color scheme as in (a−) is used.

directions of $\mathcal{M}^-$, and vice versa. The surfaces representing such initial conditions are visualized in Fig. 5. In the case of sphere with a constant radius t_i^+ in $\mathcal{M}^+$, we get

$$t_i^- \to \infty, \qquad z_i^- \to \pm\infty, \tag{44}$$

along the axis, corresponding to the diverges of (37) at the places $Z = \{0, \infty\}$ where the string ends are attached to the null cone, see the left part of Fig. 5. This divergence is in reverse translated into the shape of the initial time slices in the part (b+) of Fig. 5 leading to particles emerging simultaneously at constant time t_i^-.

Moreover, to visualize the effect of the Penrose junction condition (11) as a null cone mapping, which was schematically illustrated in Figs. 1 and 4, we plot its explicit realization for the one string case (43), see Fig. 6.

The above one-string situation can be nontrivially extended by its boosting in the perpendicular direction. The corresponding complex mapping $h(Z)$ can be constructed as a series of string creation along the z-axis, perpendicular rotation, boost, and final backward rotation, namely

$$h(Z) = \mathcal{R}_{\{-\frac{\pi}{2},0,0\}}\mathcal{B}_{\{w\}}\mathcal{R}_{\{\frac{\pi}{2},0,0\}}\mathcal{S}_{\{\delta\}}Z. \tag{45}$$

It explicitly becomes

$$h(Z) = -\frac{w - 1 - (w+1)Z^{1-\delta}}{w + 1 - (w-1)Z^{1-\delta}}. \tag{46}$$

In comparison with simple case (43), the boost-induced asymmetry is reflected in the deformation of the natural

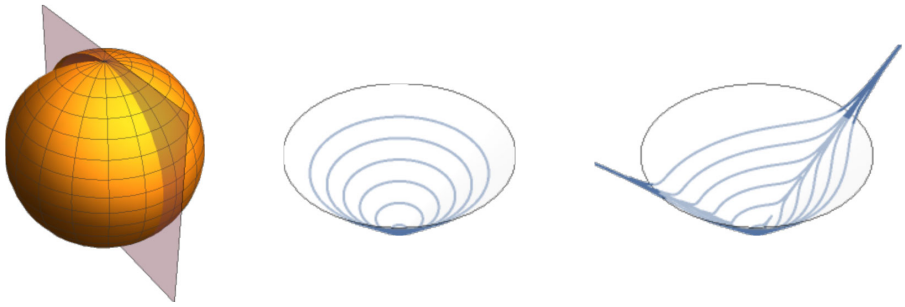

FIG. 6. The initial $t_i^+ = \text{const}$ sphere is cut by a plane passing through the origin and including both string ends (a). Since the plane does not contain the deficit angle, taking specific values t_i^+ corresponds to the full circles of test particles (b) that are lying on the null cone $\mathcal{N}$, where the time goes in the direction of the cone axis. The function $h(Z)$ then maps the initial circles (b) along the null cone $\mathcal{N}$ as in Figs. 1 and 4. In (c) we can see the resulting displacement of test particles on $\mathcal{N}$ viewed from the $\mathcal{M}^-$ region. The divergences correspond to the moving string ends related to the infinities of (37).

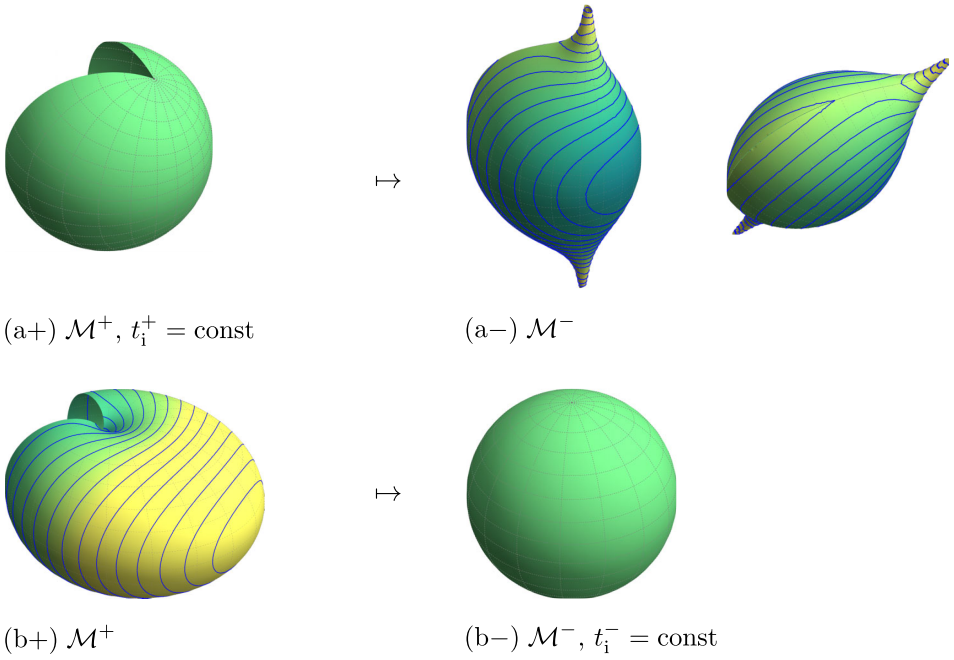

FIG. 7. Description of the plot is the same as in Fig. 5. The differences in the shape of the particles swarm interacting with the impulse are caused by the additional string motion in the x-direction related to the form of function $h(Z)$ given by (46) with the boost parameter $w = 0.6$. In the second picture in (a−) we can observe a sharp "fin" with the time equipotentials being nonsmooth. That is the region through which the string travels. In these visualizations, the relation between (a) and (b) clearly corresponds to the multiplication of the radius by a scaling factor $|h'|\frac{1+|Z_i|^2}{1+|h|^2}$. The string ends are at the north and south pole behind the wave regardless of its transversal motion.

static spherical initial data, with t_i^+ or t_i^- being constant, respectively. The transversal string motion induces another caustic formation in addition to those given by the string snapping itself. The possible initial setting is visualized in Fig. 7.

In analogy with Fig. 6, the example of an explicit null cone mapping for the moving string (46) is visualized in Fig. 8. In general, plotting such a picture requires to suppress one spatial dimension, i.e., to chose a particular spatial cut through the initial data. In the case of Fig. 8, the string ends are not included in the cut and therefore the test particles are mapped only to the finite values of t_i^-.

Finally, as a comprehensive picture characterizing the dynamical structure of boosted one-string impulsive spacetime with (46) we plot a sequence of deformations of an initially static swarm of particles. Their initial space and time displacement in the region $\mathcal{M}^+$ is chosen in such a way that they all emerge simultaneously in the region $\mathcal{M}^-$ as a sphere of constant radius t_i^-, i.e., it is described by Fig. 7(b+). Subsequently, due to the nontrivial impulsive effect, the particles gained nontrivial velocities and start moving along geodesics (straight lines) in the Minkowski background (21) with initial data given by (22) and (23), see Fig. 9. Here, the vertical deformation and particle acceleration along the z-axis are given by their attraction by

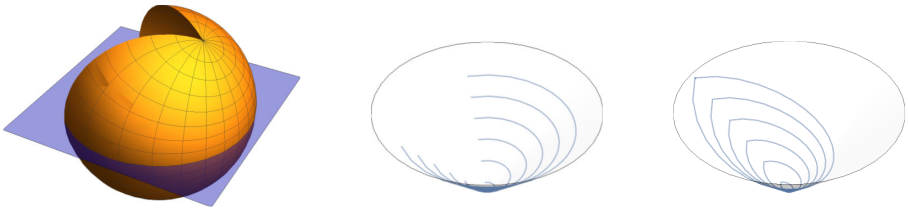

FIG. 8. The planar cut of the initial swarm of particles is visualized in analogy with Fig. 6. However, here in part (a), the plane is chosen to explicitly contain the topological defect caused by the string (b) while the string ends are out of the plane. The finlike deformation in part (c) corresponds to the string motion in the x-direction, however, it does not contain divergences since the string ends are out of our planar cut.

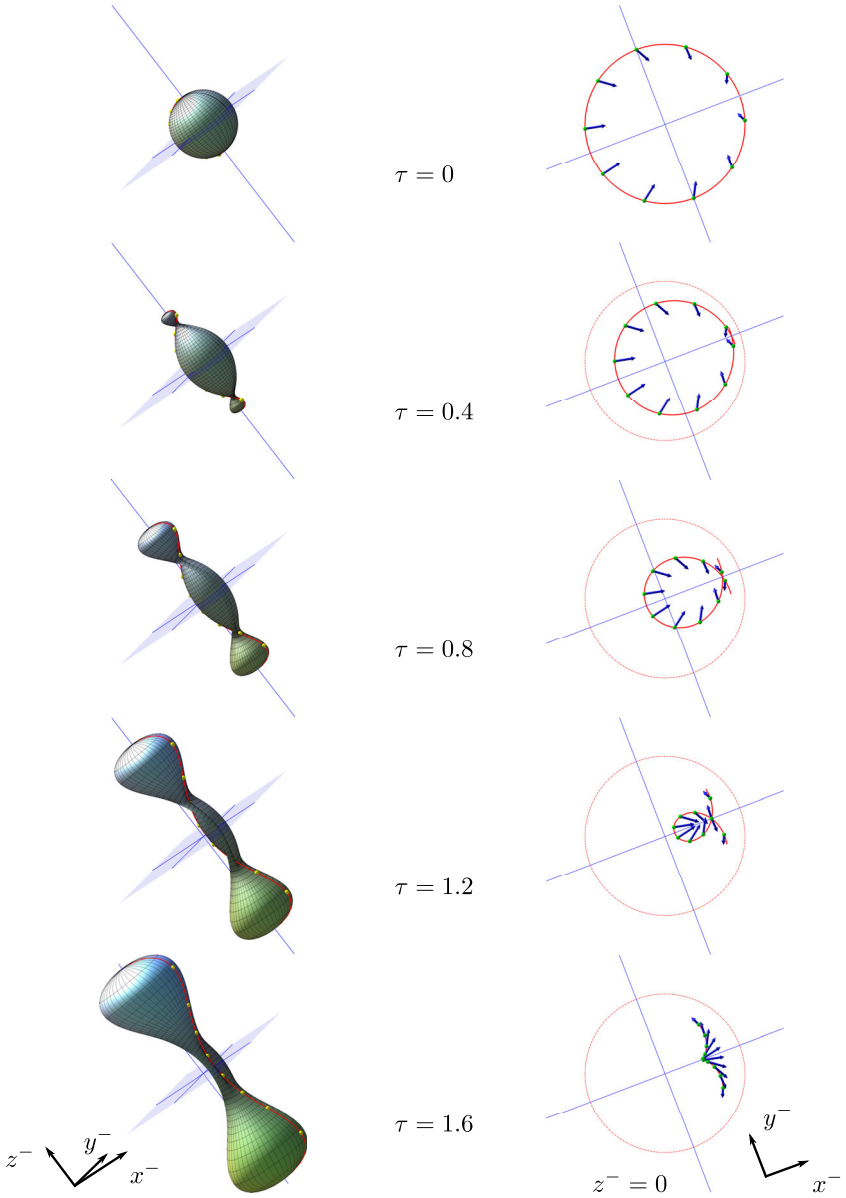

FIG. 9. The effect of snapping boosted string (46) on free-test particles initially at rest in $\mathcal{M}^+$ with positions satisfying $x_{\mathrm{i}}^{+2} + y_{\mathrm{i}}^{+2} + z_{\mathrm{i}}^{+2} = t_{\mathrm{i}}^{+2}$ such that particular choice of t_{i}^{+} leads to $t_{\mathrm{i}}^{-} = \text{const}$, i.e., the data are prepared as in the bottom part of Fig. 7 to emerge as a real sphere at given time t_{i}^{-}. However, the test observers gain nontrivial velocities. Their time evolution is plotted in the left column. To visualize the asymmetry induced by the string motion in the x-direction we show the cut by the plane $z = 0$, perpendicular to the string, in the right column.

the moving ends of the snapped string. Near poles, where the string ends are attached to the impulsive sphere, the speed of test particles reaches the speed of light. The attractive effect of the string ends results in the caustics formed by a mutual crossing of trajectories starting on opposite sides of the initial sphere with respect to the z-axis. Such behavior agrees with the simple static one-string case described in [28]. However, there is the additional horizontal asymmetry induced by the boost of the string in the x-direction. To emphasize the boost effect we plot the cut by $z = 0$ plane in the left part of Fig. 9, where the additional caustic formation due to the string transversal motion can be observed.[2]

The above discussion shows the effects of a moving snapped cosmic string on free-test observers and the way how these effects can be understood and visualized. Notice that the subcase without string boost was already studied in [27,28] considering also cosmological backgrounds. In the

[2]In the evolutionary Figs. 9, 14, 19, and 22, the color scale has no other meaning than to visualize plasticity of the spatial deformation.

subsequent section, we follow [17,26] and analyze various impulses generated by a pair of snapped strings in the same way as in the one-string case.

Naturally, in the case of boosted string one can be worried by the fact that the cut out planes are not extrinsically flat, as can be seen in Fig. 7. However, it can be analytically shown that following situations are equivalent:

(i) initially static particles and their interaction with impulse generated by a string boosted by w in the positive x-direction, i.e., $h(Z)$ given by (46); and
(ii) initially moving particles in the negative x direction with the speed $v=\frac{1-w^2}{1+w^2}$ interacting with a static string described by (43).

VI. TWO-STRING GEOMETRIES

Here, we extend the results presented in [26] and discuss their geometric properties via analysis of induced geodesic motion. To do so, an alternative sequences of basic steps entering the two-string complex mapping $h(Z)$ construction has to be employed and particular differences in the resulting motion identified.

A. Original results by Podolský and Griffiths and their generalization

The possibility of expanding impulse generated by a colliding and snapping pair of cosmic strings was originally anticipated by Nutku and Penrose in [17]. Simultaneously, there were doubts that explicit realization of the corresponding function $h(Z)$ is hard to find, however, its existence should be guaranteed by the Riemann theorem. Surprisingly, a few years later Podolský and Griffiths explicitly performed such a construction in [26]. Their simplest nonboosted two-string formula reads

$$h(Z)=\mathcal{S}_{\{\varepsilon\}}\mathcal{R}_{\{\frac{\pi}{2},\frac{\pi}{2},\frac{\pi}{2}\}}\mathcal{S}_{\{\delta\}}Z=\left(\frac{iZ^{1-\delta}-1}{Z^{1-\delta}-i}\right)^{1-\varepsilon}. \tag{47}$$

In terms of fixed Cartesian coordinates, it can be described in such a way that the string parametrized by δ and placed along the z-axis is rotated to take a place along the y-axis and the second string (encoded in ε) is then created along the z-axis. However, the construction should be more precisely understood in terms of the active Lorentz transformations (13). In particular, this can be seen from the no string limit of (47). Taking both parameters trivial, namely $\delta=0=\varepsilon$, does not provide the identity, but

$$h(Z)=\frac{iZ-1}{Z-i}, \tag{48}$$

which is exactly the residual rotation $\mathcal{R}_{\{\frac{\pi}{2},\frac{\pi}{2},\frac{\pi}{2}\}}Z$ employed within construction of (47). The Schwarzian derivative (10) is vanishing and the seemingly nontrivial position shift (22) directly shows the unphysical rotation or the artificial identification of the background Cartesian frame. However, to directly gain all relevant information about test particles interacting with the impulse from the refraction formulas (22) and (23), it is important and useful to remove such a coordinate discrepancy. Before we do that, let us also show the ultimate result of [26], which adds a boost to the simplest interaction of static strings (47), and therefore, it was interpreted as the collision of strings that induces their snap and subsequent creation of the impulse. The particular complex mapping reads

$$h(Z)=w_2\frac{h_c^{1-\varepsilon}-1}{h_c^{1-\varepsilon}+1} \tag{49}$$

with

$$h_c(Z)=-\frac{(w_1-i)Z^{1-\delta}+(w_1+i)}{(w_1+i)Z^{1-\delta}+(w_1-i)}. \tag{50}$$

As in the case of (47), setting $w_1=1=w_2$ and $\delta=0=\varepsilon$ do not provide an identical mapping, and therefore, it can not be directly employed in the refraction formulas (22) and (23).

Now, we remove the artificial coordinate effect in (47), and subsequently also in (49), and include an addition boost to the overall mapping, which will be important within the subsequent discussion. In particular, let us perform the following sequence of mappings, namely

$$h_0(Z)=Z, \tag{51}$$

$$h_1(Z)=\mathcal{S}_{\{\delta\}}h_0(Z), \tag{52}$$

$$h_2(Z)=\mathcal{B}_{\{w_2\}}\mathcal{R}_{\{\frac{\pi}{2},\frac{\pi}{2},\pi\}}h_1(Z), \tag{53}$$

$$h_3(Z)=\mathcal{B}_{\{w_3\}}\mathcal{R}_{\{-\frac{\pi}{2},0,0\}}h_2(Z), \tag{54}$$

$$h_4(Z)=\mathcal{S}_{\{\varepsilon\}}h_3(Z), \tag{55}$$

$$h_5(Z)=\mathcal{B}_{\{w_5\}}\mathcal{R}_{\{\frac{\pi}{2},\frac{\pi}{2},\frac{\pi}{2}\}}h_4(Z). \tag{56}$$

These operations can be geometrically understood in terms of the Riemann sphere, see Figs. 10 and 11 for the special cases, while the fully general mapping takes the form

$$h(Z)=iw_5\frac{-1+i\left(w_3\frac{(i+w_2)Z^{\delta}-(i-w_2)Z}{(i-w_2)Z^{\delta}-(i+w_2)Z}\right)^{1-\varepsilon}}{1+i\left(w_3\frac{(i+w_2)Z^{\delta}-(i-w_2)Z}{(i-w_2)Z^{\delta}-(i+w_2)Z}\right)^{1-\varepsilon}}, \tag{57}$$

which naturally becomes identical for trivial boosts and deficit angles, i.e., $w_j=1$ and $\delta=0=\varepsilon$. The simplest

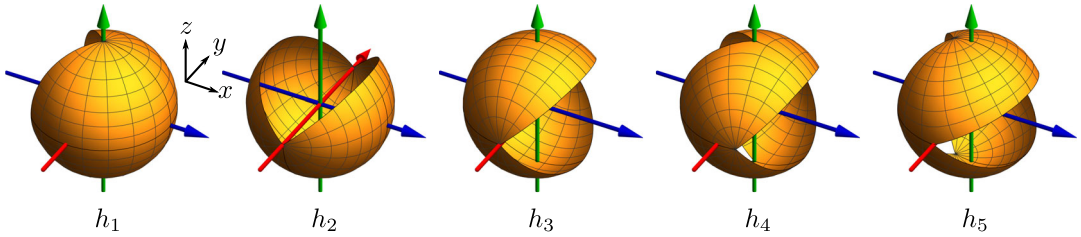

FIG. 10. A sequence of elementary mappings (51)–(56) employed within the construction of the function (57) encoding interaction of two cosmic strings and their snap. Here we plot the simplest case $w_2 = w_3 = w_5 = 1$ directly improving (47). The function $h(Z)$ then enters the junction conditions (11) of two half-spaces "in front of" and "behind" the impulsive wave. Interestingly, the second string creation, step $h_3 \to h_4$, inherently induces an additional boost. This can be counterbalanced by a specific choice of w_j, see Fig. 11.

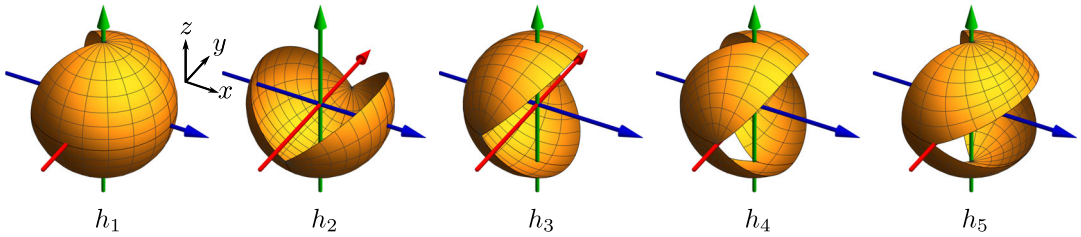

FIG. 11. The same sequence of elementary mappings as in Fig. 10. However, here we decided to take $w_2 = \tan\frac{\pi}{4(1-\varepsilon)}$, see (60), and $w_3 = 1 = w_5$ so that the additional inherent boost in $h_3 \to h_4$ is compensated and the strings are placed along the axes, compare h_4 steps.

"static" interaction[3] of the strings is then described by choosing $w_2 = w_3 = w_5 = 1$ in (57) which then corresponds to (47) with the artificial coordinate rotation removed, namely

$$h(Z) = i\frac{-1 + i\left(-i\frac{1-iZ^{1-\delta}}{1+iZ^{1-\delta}}\right)^{1-\varepsilon}}{1 + i\left(-i\frac{1-iZ^{1-\delta}}{1+iZ^{1-\delta}}\right)^{1-\varepsilon}}, \tag{58}$$

while for a specific choice of boosts w_j we may obtain an improved version of (49). On a general level, the location of ends of the strings for (57) is given by

$$Z = \left\{0, \infty, \left(\frac{i+w_2}{i-w_2}\right)^{\frac{1}{1-\delta}}, \left(\frac{i-w_2}{i+w_2}\right)^{\frac{1}{1-\delta}}\right\}. \tag{59}$$

Here, let us also emphasize the important observation that the elementary operation $\mathcal{S}_{\{\varepsilon\}}$, see (55), which creates the second string placed along z-axis, inherently shifts the position in the x-direction of the already existing string. In Fig. 10, this corresponds to the step $h_3 \to h_4$, where the sphere is distorted and the existing string is effectively boosted in the x-direction.

[3]To be more precise, this case is static only in terms of the boost parameters w_j, however, the second string creation induces the additional inherent boost as we will discuss later.

We can counterbalance this effect by the newly introduced additional boost in the opposite direction, namely

$$w_2 = \tan\frac{\pi}{4(1-\varepsilon)}, \tag{60}$$

and $w_3 = 1 = w_5$, see Fig. 11 and changes in the sequence $h_2 \to h_3 \to h_4$.

The resulting nodal points are then aligned with the axes and there is no transversal velocity (as could be seen from their action on test particles). These situations are also compared in Fig. 12 which visualizes structure of the Riemann sphere cuts with respect to w_2.

The discussion of an additional boost is connected with the real location of the strings viewed from the region behind the wave. Geometrically, after cutting out two wedges (deficit angles) we are glueing the corresponding "lips" back together, however, it is done in a particular order. Here, the string governed by parameter δ remains straight along the z-axis, while using (59) the string parts governed by ε, and lying in the x-y plane, can be identified by the polar angle ϕ_s, namely

$$\phi_s = \pm\frac{\pi - \arg\frac{w_2+i}{w_2-i}}{1-\delta}. \tag{61}$$

In the case with (60) and $w_3 = 1 = w_5$, i.e., the constants are set so that there is no transversal motion of the strings, pieces of one string are attached to the north and south

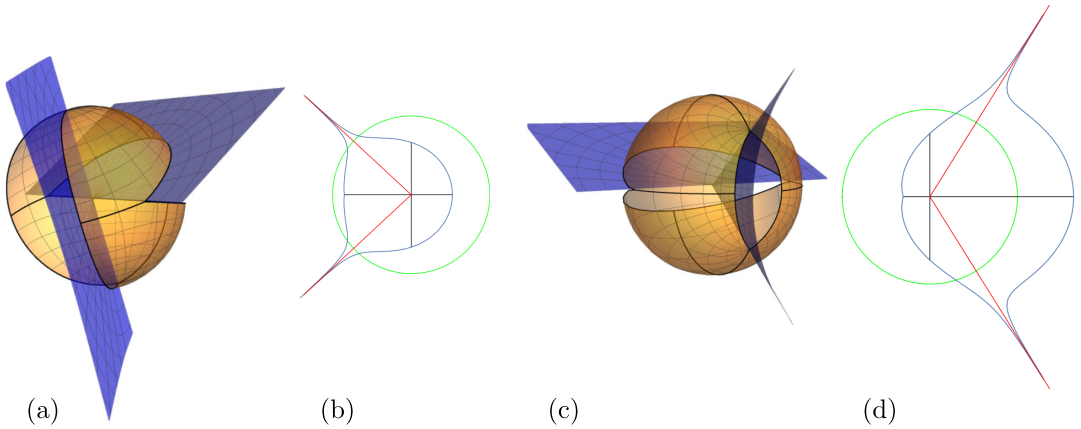

FIG. 12. In part (a) we plot the Riemann sphere as in Fig. 11 h_5, i.e., corresponding to the mapping (57) with $w_2 = \tan\frac{\pi}{4(1-\epsilon)}$ compensating the additional boost. The cut by x-y plane of the $t_{\rm i}^+ = \text{const}$ initial condition image in $\mathcal{M}^-$ [see Fig. 13(a−)] is shown in part (b). The string ends follow the red lines, whose mutual angle is given by (61). The same situations with a generic boost $w_2 = 0.4$ are visualized in (c) and (d). In (a) and (c) we plot the blue surfaces given by parametrization of the wedge edges. If there is no transversal motion of the strings, the surfaces are planes with vanishing extrinsic curvature, while in the case of boosted strings, the situation becomes more complicated.

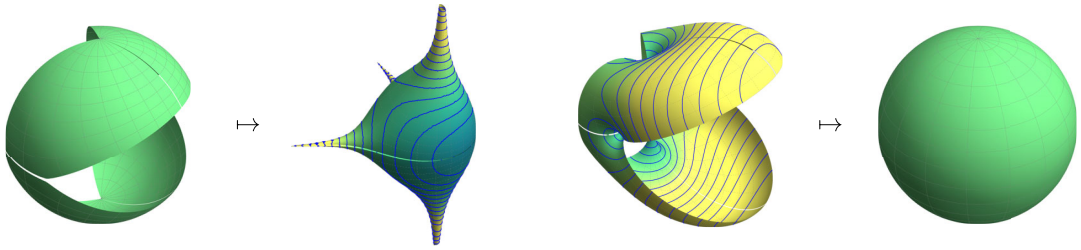

FIG. 13. As in Fig. 5 two natural sets of static initial data are prepared for the improved two-string case (57) with $w_3 = 1 = w_5$ and w_2 given by (60). The plot of the initial condition for the original mapping (47) would differ by rotation and a trivial choice $w_2 = 1$.

pole, respectively, while the second string ends form the mutual angle

$$\Delta\phi = \left(2 - \frac{1}{2(1-\delta)(1-\varepsilon)}\right)\pi, \tag{62}$$

which is found as a direct application of the general formula (61).

Finally, based on the geodesic motion let us describe the effect of an impulse generated by (58). We visualize its interaction with initially static test particles prepared in $\mathcal{M}^+$ to emerge synchronously on a sphere in $\mathcal{M}^-$, see the right part of Fig. 13 identifying the initial data and Fig. 14 depicting the overall deformation caused by the impulse. The shape evolution corresponds to the straight motion on a flat background. As in the previous one-string case, the test particles are dragged by the moving string ends and by the boost of the string itself. Obviously, there is a nontrivial distribution of their velocities given by (23). Using these formulas, the speed of a given particle can be evaluate as

$$v^- = \sqrt{(v_x^-)^2 + (v_y^-)^2 + (v_z^-)^2} \tag{63}$$

with

$$(v_x^-, v_y^-, v_z^-) \equiv \left(\frac{\dot{x}_{\rm i}^-}{\dot{t}_{\rm i}^-}, \frac{\dot{y}_{\rm i}^-}{\dot{t}_{\rm i}^-}, \frac{\dot{z}_{\rm i}^-}{\dot{t}_{\rm i}^-}\right). \tag{64}$$

Such a distribution is plotted in Fig. 15, which again indicates the string end locations since in their neighborhood the test particles approach the speed of light.

B. Peculiar form of the simple two-string mapping

In this part, let us derive an alternative form of the function $h(Z)$ in the case of a pair of cosmic strings, which should demonstrate the subtlety of the construction process.

Let us start with the sequence of elementary steps

$$h_0(Z) = Z, \tag{65}$$

$$h_1(Z) = \mathcal{B}_{\{w_3\}}\mathcal{S}_{\{\delta\}}h_0(Z), \tag{66}$$

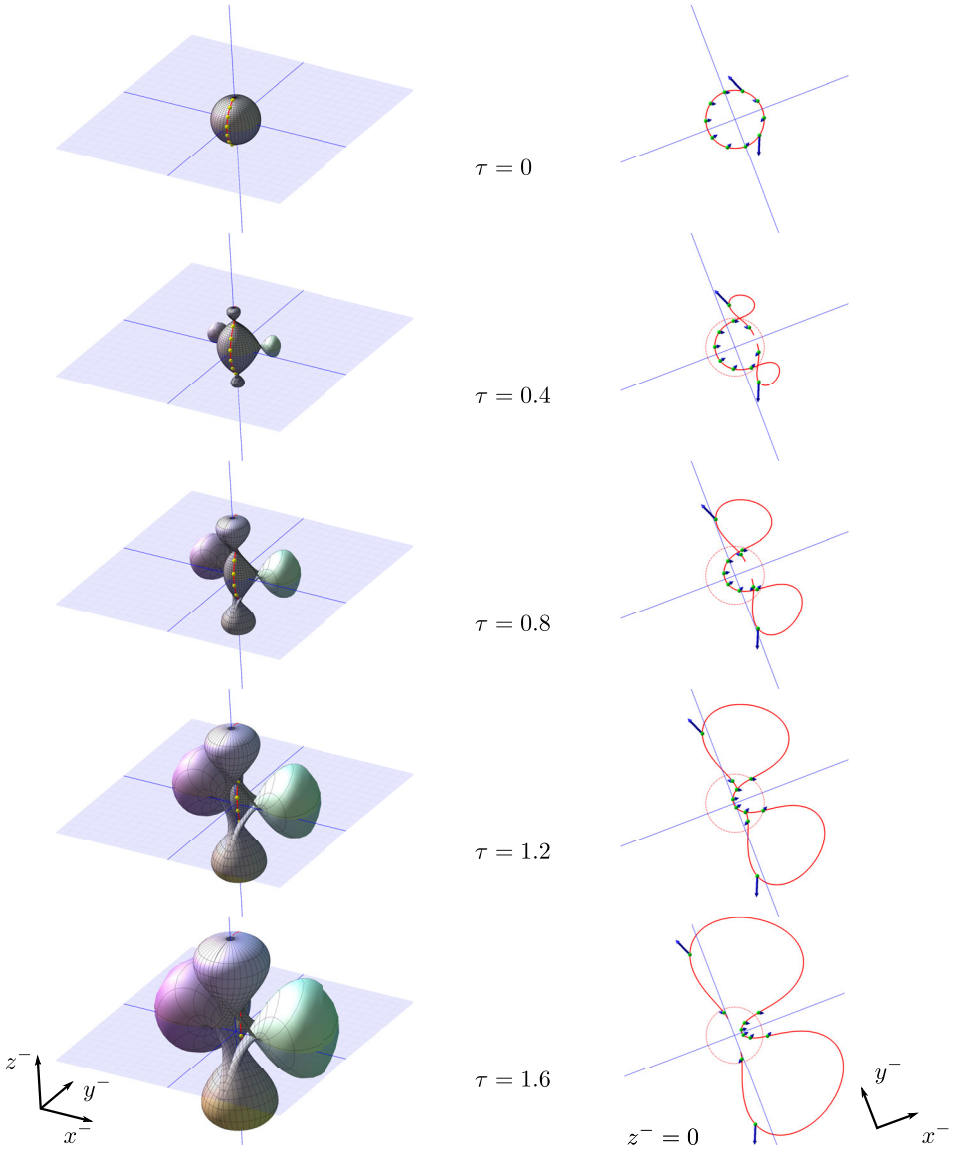

FIG. 14. In analogy with Fig. 9 we plot a burst of test particles hit by the impulsive wave generated by the improved mapping (58), which can be directly used in refraction formulas (22) and (23) entering geodesics (21). This choice is visualized in Fig. 10. The employed initial conditions represent static particles in front of the wave displaced to emerge synchronously at constant time. The typical values $\delta = \frac{1}{4}$ and $\varepsilon = \frac{1}{8}$ are used. We observe the dragging of test particles in the directions of four moving ends of the snapped string pairs. This is combined with inherent (noncompensated) boost in the x-direction induced by the second string creation.

$$h_2(Z) = \mathcal{R}_{\{\frac{\pi}{2},0,0\}} h_1(Z), \tag{67}$$

$$h_3(Z) = \mathcal{B}_{\{w_7\}} \mathcal{S}_{\{\varepsilon\}} h_2(Z), \tag{68}$$

$$h_4(Z) = \mathcal{R}_{\{-\frac{\pi}{2},0,0\}} h_3(Z), \tag{69}$$

which leads to the mapping

$$h(Z) = -\frac{1 - w_7 \left(\frac{1+w_3 Z^{1-\delta}}{1-w_3 Z^{1-\delta}}\right)^{1-\varepsilon}}{1 + w_7 \left(\frac{1+w_3 Z^{1-\delta}}{1-w_3 Z^{1-\delta}}\right)^{1-\varepsilon}}. \tag{70}$$

Surprisingly, we identify only three string ends located at

$$Z = \left\{0, \infty, w_3^{-\frac{1}{1-\delta}}\right\}. \tag{71}$$

The sequence (65)–(69) thus cuts out the wedge $2\pi\delta$ along the z-axis and performs a boost, makes rotation about y-axis, applies another stringlike cut parametrized by ε along the original x-axis with another boost, and finally rotates backwards about unchanged y-axis. The simplified construction is visualized in Fig. 16. The mapping then leads to identity for $\delta = 0 = \varepsilon$ and $w_3 = 1 = w_7$.

Similarly to in the previous section and the case of mapping (57) as shown in Fig. 12, the second-string

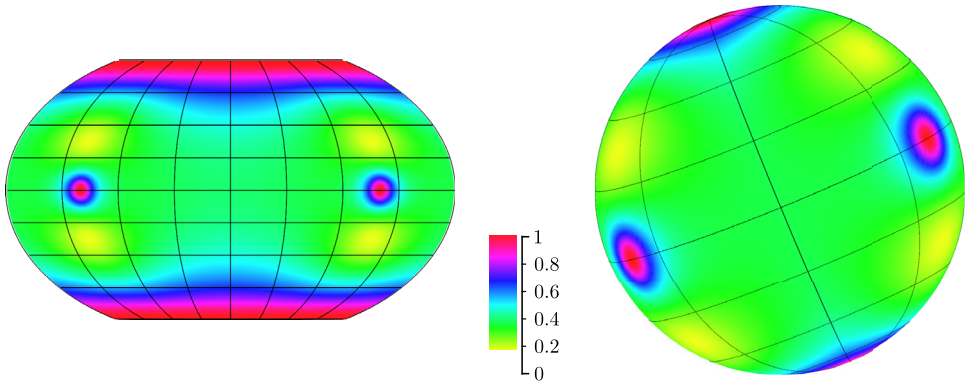

FIG. 15. The speed distribution of the test particles (63) in the region behind the impulse. The initially static particles in front of the impulse emerging simultaneously behind the wave generated by (58) are considered with the typical values $\delta = \frac{1}{4}$ and $\varepsilon = \frac{1}{8}$ of the deficit parameters. In such a case, the minimal gained speed is 0.18 in yellow regions and reaches the speed of light near the four string ends colored by red. Here, we show the Kavrayskiy VII projection (left) and the spatial scheme (right).

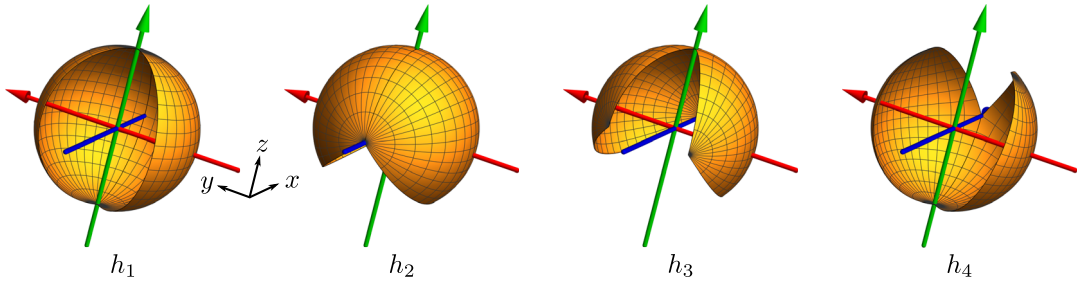

FIG. 16. Particular steps of the construction of peculiar mapping (70) simplified by assuming trivial boost parameters $w_3 = 1 = w_7$.

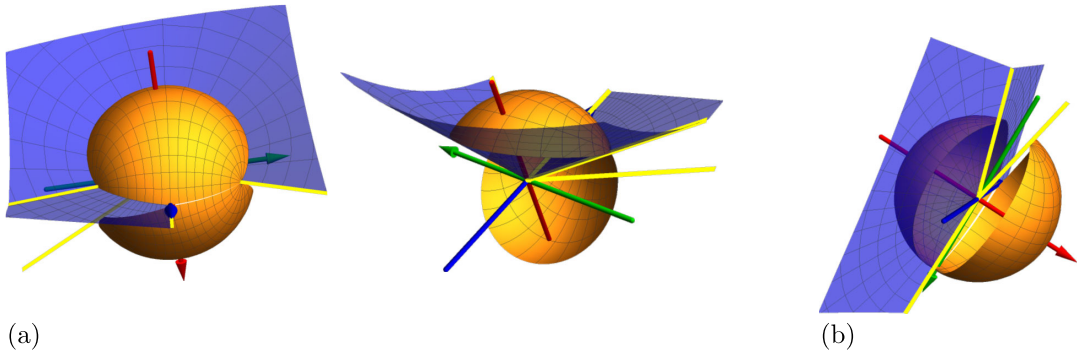

FIG. 17. In the case of generic boosts, one surface swept by the Riemann sphere edge has nonvanishing extrinsic curvature, while the second one is a trivial plane, see two views in part (a). In the static case, given by the boost choice (72), all the surfaces are planar. The pictures are reflectively symmetric with respect to the $y = 0$ plane corresponding to the blue and green axis.

creation induces an additional boost. Then the edges of Riemann sphere cutouts, parametrized by V, represent a generic curved surface. The corresponding extrinsic curvature vanishes and the surface becomes a plane if the inherent boost is compensated by a suitable choice of the artificial boosts in our construction. In particular, taking

$$w_3 = 1, \qquad w_7 = \sqrt{\frac{1 - \sin\frac{\varepsilon\pi}{2}\left(\tan\frac{\delta\pi}{2}\right)^{-(1-\varepsilon)}}{1 - \sin\frac{\varepsilon\pi}{2}\left(\tan\frac{\delta\pi}{2}\right)^{+(1-\varepsilon)}}}, \tag{72}$$

guarantees that the strings do not move in the transverse direction at all. This is illustrated in Fig. 17.

Based on the construction (65)–(69) with two string-like operations, one would naively expect that it describes a pair of perpendicular cosmic strings with four moving ends after their snap. However, inspecting (71) and the static initial data choice in Fig. 18, we may conclude that there are only three string pieces. This is exactly the above-mentioned subtlety in the $h(Z)$ construction. One part of the first string disappears by the creation of the second string (68) which removes

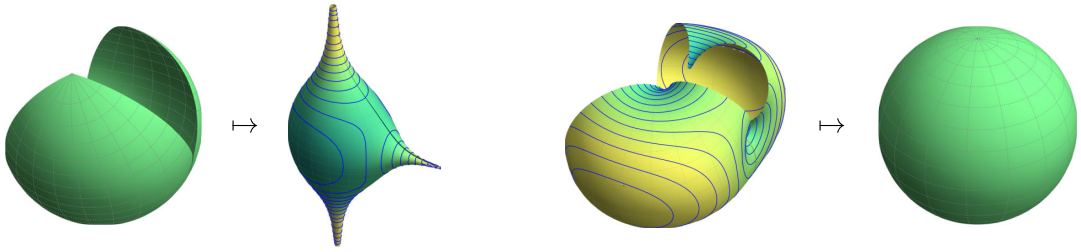

FIG. 18. The static initial data choice for the simplified complex mapping (70) with $w_3 = 1 = w_7$. The infinities in the part (a−) indicate the presence of only three moving string pieces.

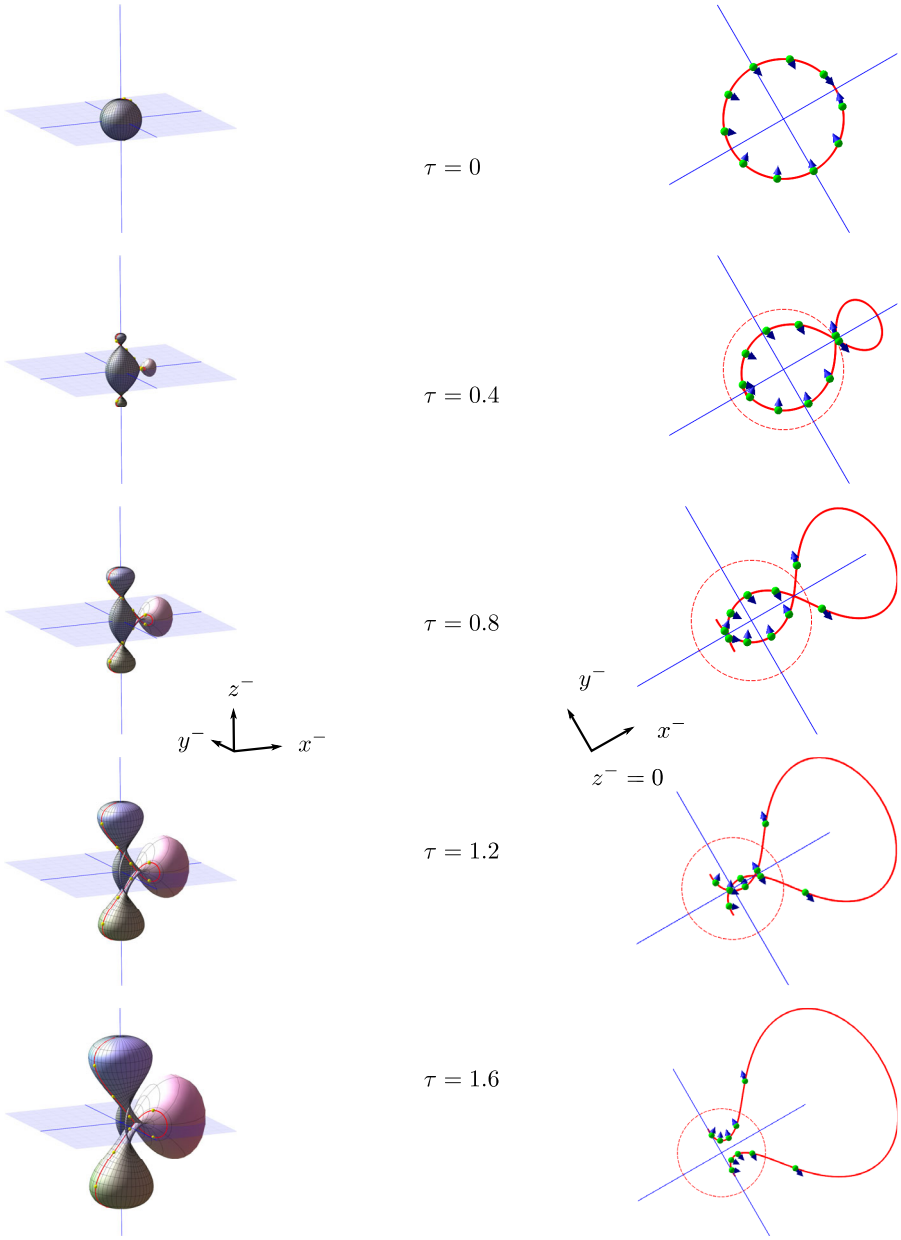

FIG. 19. Deformation of an initially static swarm of particles that emerge instantly as a sphere of constant radius $t_{\rm i}^-$. The impulse is generated by (70) with $w_3 = 1 = w_7$ and string parameters $\delta = \frac{1}{4}$, $\varepsilon = \frac{1}{8}$. The asymmetry in the resulting motion of test particles is caused by the absence of one semi-infinite cosmic string along the negative x-axis and a boost induced by the second string creation.

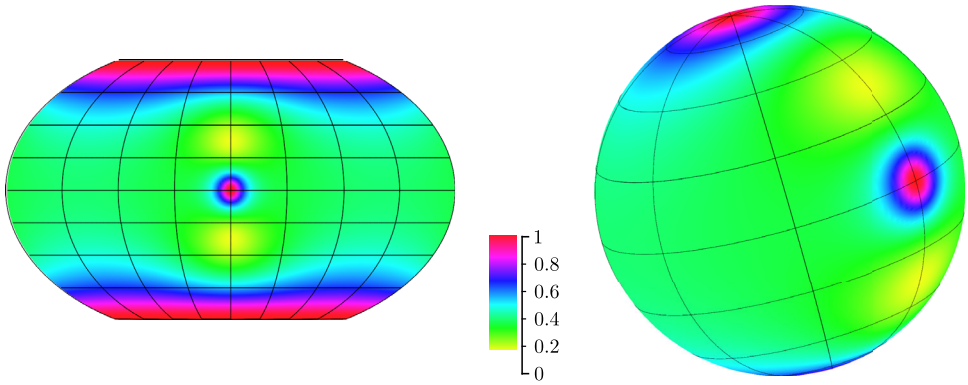

FIG. 20. In analogy with Fig. 15, the speed distribution (63) of initially static test particles, simultaneously escaping the impulsive surface, is plotted. Here, the impulse is generated by (70) with $w_3 = 1 = w_7$ and $\delta = \frac{1}{4}$, $\varepsilon = \frac{1}{8}$. The color scale stars at the minimal gained value 0.18. There are only three regions with the speed approaching the speed of light corresponding to three moving string pieces, see the Kavrayskiy VII projection (left) and the spatial picture (right).

the associated nodal point of the Riemann sphere, see $h_2 \to h_3$ in Fig. 16.

Finally, we can visualize the kinematic effect of the impulse generated by (70) with $w_3 = 1 = w_7$ on the motion of initially static test observers, see Fig. 19 for the evolution picture and Fig. 20 for the speed distribution. Due to the absence of a string piece along the negative x-axis and noncompensated inherent boost the resulting picture is asymmetric. Without an appropriate global view, one may be confused. In particular, restricting the analysis to just a quarter of the picture including two perpendicular string pieces in the positive x- and z-directions, and taking the deficit parameters $\delta = \varepsilon$ one would expect a symmetric picture in the presumed case of a pair of complete strings with four ends. However, we observe an induced motion of test particles that prefers the single-end direction.

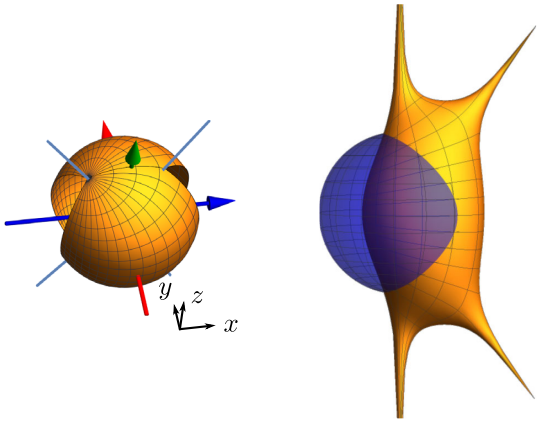

FIG. 21. For the two parallel string configuration (73) we plot the resulting unit Riemann sphere mapping in $\mathcal{M}^+$ (left) where the string ends are visualized in light blue. Divergences of its image (right) in $\mathcal{M}^-$ indicate motion and mutual angles between these ends. In the right picture, we also plot the unit sphere in dark blue to represent the scaling.

C. Two parallel strings

As a last example let us briefly introduce $h(Z)$ representing two parallel strings. By the definition, they cannot be made standing simultaneously. Therefore, the straightforward idea is to create the first (generically boosted) string, apply the rotation and another boost to induce its motion in the perpendicular direction, rotate back and create the second parallel string again with a generic boost. The relevant sequence in terms of elementary operations is

$$h(Z) = \mathcal{R}_{\{\pi/2,0,0\}}\mathcal{B}_{\{w_{10}\}}\mathcal{R}_{\{-3\pi/2,0,0\}}\mathcal{S}_{\{\varepsilon\}}\mathcal{R}_{\{3\pi/2,0,0\}} \times \mathcal{B}_{\{w_5\}}\mathcal{R}_{\{3\pi/2,0,0\}}\mathcal{B}_{\{w_3\}}\mathcal{S}_{\{\delta\}}Z, \tag{73}$$

with the string ends given by

$$Z = \left\{0, \infty, \left(\frac{1}{w_3}\frac{1+w_5}{1-w_5}\right)^{\frac{1}{1-\delta}}, \left(\frac{1}{w_3}\frac{1-w_5}{1+w_5}\right)^{\frac{1}{1-\delta}}\right\}. \tag{74}$$

The mapping (73) could be analyzed in the same way as in two previous cases. Here, we only show the effect of such a mapping in terms of the Riemann sphere and deformation of the related $t_1^+ = \text{const}$ spherical initial data, see Fig. 21.

The physical interpretation of the above construction (73) can be directly deduced from the resulting motion of initially static test particles, see Fig. 22. The deformation is again induced by the dragging of geodesics due to the motion of the string ends.

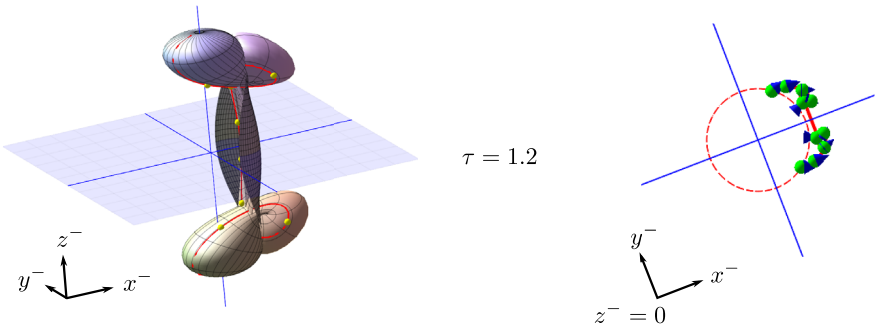

FIG. 22. The initially static spherical distribution of test particles interacts with the expanding impulse generated by (73) corresponding to a snapped pair of parallel cosmic strings. The only one typical evolution step of such a distribution along geodesics (21) is depicted.

VII. CONCLUSIONS

We studied geometries representing expanding impulsive gravitational waves. Our main aim was a geometric description and physical interpretation of the complex mapping $h(Z)$ entering the Penrose junction conditions (11). In particular, situations related to the stringlike nature of the wave source were elaborated. The $h(Z)$ properties and its refractive effects were connected with the motion of free test particles crossing the null wave surface. This was possible due to employing the recent rigorous results on the geodesic motion in expanding impulses. To clarify the role of elementary steps in $h(Z)$ construction, we analyzed specific initially static classes of geodesic congruences. Such an approach was introduced in the case of boosted one string as the simplest possibility. Subsequently, it was followed by three situations with two strings, where we clarified and extended previous results. In particular, we studied a snapping pair of cosmic strings, its degenerate subclass with only three string pieces generating the impulse, and finally, a case of two parallel strings. In general, the effects of expanding impulses generated by snapped cosmic strings acting onto geodesic motion can be described as a dragging of test particles by the string ends and induced motion in their directions. This analysis also showed nontrivial inherent boostlike effects within the construction of the two-string scenarios and the way of its compensation.

ACKNOWLEDGMENTS

D. K. acknowledges the support of the Czech Science Foundation, Grant No. GAČR 21-11268S. R. Š. was supported by the Czech Science Foundation Grant No. GAČR 22-14791S.

[1] A. Einstein, Näherungsweise Integration der Feldgleichungen der Gravitation, Sitzungsber. Preuss. Akad. Wiss. Phys. Math. Kl. 688 (1916).
[2] A. Einstein, Über Gravitationwellen, Sitzungsber. Preuss. Akad. Wiss. Phys. Math. Kl. **1**, 154 (1918).
[3] F. A. E. Pirani, Invariant formulation of gravitational radiation theory, Phys. Rev. **105**, 1089 (1957).
[4] H. Bondi, Plane gravitational waves in general relativity, Nature (London) **179**, 1072 (1957).
[5] R. A. Hulse and J. H. Taylor, Discovery of a pulsar in a binary system, Astrophys. J. **195**, L51 (1975).
[6] B. P. Abbott *et al.* (LIGO Scientific and Virgo Collaborations), Observation of Gravitational Waves from a Binary Black Hole Merger, Phys. Rev. Lett. **116**, 061102 (2016).
[7] B. P. Abbott *et al.* (LIGO Scientific and Virgo Collaborations), GW170817: Observation of Gravitational Waves from a Binary Neutron Star Inspiral, Phys. Rev. Lett. **119**, 161101 (2017).
[8] I. Robinson and A. Trautman, Spherical Gravitational Waves, Phys. Rev. Lett. **4**, 431 (1960).
[9] I. Robinson and A. Trautman, Some spherical gravitational waves in general relativity, Proc. R. Soc. A **265**, 463 (1962).
[10] W. Kundt, The plane-fronted gravitational waves, Z. Phys. **163**, 77 (1961).
[11] W. Kundt, Exact solutions of the field equations: Twist-free pure radiation fields, Proc. R. Soc. A **270**, 328 (1962).
[12] H. Stephani, D. Kramer, M. MacCallum, C. Hoenselaers, and E. Herlt, *Exact Solutions of Einstein's Field Equations* (Cambridge University Press, Cambridge, England, 2003), 2nd ed.
[13] J. B. Griffiths and J. Podolský, *Exact Space-Times in Einstein's General Relativity* (Cambridge University Press, Cambridge, England, 2009).
[14] M. Grosser, M. Kunzinger, M. Oberguggenberger, and R. Steinbauer, *Geometric Theory of Generalized Functions*, Mathematics and its Applications Vol. 537 (Kluwer, Dordrecht, 2001).
[15] R. Steinbauer and J. A. Vickers, The use of generalized functions and distributions in general relativity, Classical Quantum Gravity **23**, R91 (2006).

[16] R. Penrose, The geometry of impulsive gravitational waves, in *General Relativity*, edited by L. O'Raifeartaigh (Clarendon Press, Oxford, 1972), pp. 101–115.
[17] Y. Nutku and R. Penrose, On impulsive gravitational waves, Twistor Newslett. **34**, 9 (1992).
[18] P. A. Hogan, A spherical gravitational wave in the de Sitter universe, Phys. Lett. A **171**, 21 (1992).
[19] J. Podolský and J. B. Griffiths, Expanding impulsive gravitational waves, Classical Quantum Gravity **16**, 2937 (1999).
[20] P. A. Hogan, Imploding-exploding gravitational waves, Lett. Math. Phys. **35**, 277 (1995).
[21] A. N. Aliev and Y. Nutku, Impulsive spherical gravitational waves, Classical Quantum Gravity **18**, 891 (2001).
[22] M. Hortacsu, Quantum fluctuations in the field of an impulsive spherical gravitational wave, Classical Quantum Gravity **7**, L165 (1990); **9**, 799(E) (1992).
[23] M. Hortacsu, Vacuum fluctuations for spherical gravitational impulsive waves, Classical Quantum Gravity **13**, 2683 (1996).
[24] J. Podolský, Exact impulsive gravitational waves in spacetimes of constant curvature, in *Gravitation: Following the Prague Inspiration*, edited by O. Semerák, J. Podolský, and M. Žofka (World Scientific, Singapore, 2002), pp. 205–46.
[25] J. Podolský, C. Sämann, R. Steinbauer, and R. Švarc, The global uniqueness and C^1-regularity of geodesics in expanding impulsive gravitational waves, Classical Quantum Gravity **33**, 195010 (2016).
[26] J. Podolský and J. B. Griffiths, The collision and snapping of cosmic strings generating spherical impulsive gravitational waves, Classical Quantum Gravity **17**, 1401 (2000).
[27] J. Podolský and R. Steinbauer, Geodesics in spacetimes with expanding impulsive gravitational waves, Phys. Rev. D **67**, 064013 (2003).
[28] J. Podolský and R. Švarc, Refraction of geodesics by impulsive spherical gravitational waves in constant-curvature spacetimes with a cosmological constant, Phys. Rev. D **81**, 124035 (2010).
[29] R. Steinbauer, Every Lipschitz metric has $\mathcal{C}^1$-geodesics, Classical Quantum Gravity **31**, 057001 (2014).
[30] A. F. Filippov, *Differential Equations with Discontinuous Righthand Sides* (Kluwer Academic Publishers, Dordrecht, 1988).
[31] J. Cortés, Discontinuous dynamical systems, IEEE Control Syst. Mag. **28**, 36 (2008).
[32] J. Podolský, C. Sämann, R. Steinbauer, and R. Švarc, The global existence, uniqueness and C^1-regularity of geodesics in nonexpanding impulsive gravitational waves, Classical Quantum Gravity **32**, 025003 (2015).